



Piezoelectric effect-assisted Z-scheme heterojunction ZnIn₂S₄/BaTiO₃ for improved photocatalytic reduction of CO₂ to CO

Shanyue Lu^{a,b,c,1}, Shengwei Zhang^{b,c,1}, Linlin Li^{a,b,c}, Cong Liu^{b,c,*}, Zhou Li^{b,c,*}, Dan Luo^{b,c,*}

^a School of Chemistry and Chemical Engineering, Guangxi University, Nanning 530004, China

^b Beijing Institute of Nanoenergy and Nanosystems, Chinese Academy of Sciences, Beijing 101400, China

^c School of Nanoscience and Engineering, University of Chinese Academy of Sciences, Beijing 100049, China

ARTICLE INFO

Keywords:

ZnIn₂S₄
BaTiO₃
Z-scheme
Photocatalysis
CO₂ reduction
Piezoelectric effect

ABSTRACT

Converting CO₂ into high-value-added chemicals by artificial photosynthesis technology effectively solves environmental problems and energy shortages. Nevertheless, it remains challenging to improve CO₂ conversion rates due to low photo-utilization and rapid electron-hole recombination. In this study, we successfully synthesized direct Z-scheme ZnIn₂S₄/BaTiO₃ heterojunction structure by a hydrothermal method. Specifically, compared with previous studies of various heterojunction catalysts, ZnIn₂S₄/BaTiO₃ heterojunction structure achieved a remarkably high yield of 105.89 μmol g⁻¹ h⁻¹, increasing 2.55 and 3.62-fold over the individual performance of ZnIn₂S₄ and BaTiO₃, respectively. Our investigation of photocatalytic mechanism suggest that the improved photocatalytic CO₂ reduction performance can be attributed to the synergistic effects of the piezoelectric effect and Z-scheme electron transfer mechanism. These effects can synergistically enhance space charge separation and retain photogenerated electrons, thereby facilitating a more efficient CO₂ reduction process. Consequently, this innovative piezoelectric effect-assisted Z-scheme heterojunction demonstrates immense potential to offer a novel strategy for addressing CO₂ reduction challenges and advancing sustainable energy development.

1. Introduction

As human society continues to evolve, the demand for non-renewable fossil fuels is on the rise. A sharp increase in CO₂ emissions has been caused by the excessive usage of these fossil fuels, contributing to the greenhouse effect and global environmental degradation [1–4]. In response, photocatalytic CO₂ reduction (PCR) emerges as a promising prescription to address environmental issues and mitigate energy crises by harnessing the boundless power of solar energy to reduced CO₂ waste gas into available chemicals [5–12]. To date, large amounts of materials, including metal oxides (e.g., ZnO, WO₃), sulfides (e.g., CdS), MXenes (e.g., Ti₃C₂), and others, have been extensively applied to the realm of PCR [13–20]. Nevertheless, their performance still requires enhancement due to challenges associated with low photo-utilization rates and rapid electron-hole recombination, resulting in meager CO₂ conversion rates that fall short of meeting industrial standards [21–27].

As a classical ternary metal sulfide, ZnIn₂S₄ is considered one of the

most promising catalysts in photocatalysis due to its simple synthesis process, high stability, and suitable energy band structure. However, the low photo-utilization rate and the susceptibility of electron-hole complexation severely limit the PCR performance of ZnIn₂S₄ [28,29]. Currently, the construction of heterojunctions stands as a conventional yet effective strategy to broaden the light absorption spectrum and mitigate electron-hole recombination. Nevertheless, in the classic type-II heterojunction system, carriers migrate from high conduction band (CB) semiconductors to low CB semiconductors, while holes move to semiconductors with higher valence band (VB) for carrier separation, yet at the expense of the redox capacity of photocatalyst [30,31]. In contrast, the direct Z-scheme photocatalysts facilitate photogenerated electrons transfer at the interface between low-potential CB and low-potential VB, overcoming electrostatic repulsion and promoting photo-induced carrier separation. This arrangement maintains high potentials in both CB and VB, thereby endowing the photocatalysts with excellent redox capabilities [30,32–34].

* Corresponding authors at: Beijing Institute of Nanoenergy and Nanosystems, Chinese Academy of Sciences, Beijing 101400, China.

E-mail addresses: liucong@binn.cas.cn (C. Liu), zli@binn.cas.cn (Z. Li), luodan@binn.cas.cn (D. Luo).

¹ Shanyue Lu and Shengwei Zhang contributed equally to this manuscript.

It was discovered that when piezoelectric materials are subjected to external forces (ultrasonic radiation, mechanical agitation, ball milling, or wind, etc.), the lattice of the material deforms, resulting in a piezoelectric effect [35–38], and at the same time, the centers of the positive and negative charges will also be moved in the opposite direction under the action of the stress to form a dynamic internal electric field. The electrons and holes can be continuously separated and attracted to the opposing surfaces to achieve the purpose of charge separation [39]. BaTiO₃ is considered an excellent chalcogenide piezoelectric material due to its excellent piezoelectric coefficient [40]. However, BaTiO₃ has a low carrier concentration, which leads to its poor catalytic effect. Therefore, constructing a Z-scheme ZnIn₂S₄/BaTiO₃ heterojunction is expected to offset the disadvantages of the two with each other. The internal polarization field induced by the piezoelectric response and the interfacial electric field at the heterojunction interface can synergistically promote charge transfer and segregation, resulting in excellent synergistic effects in piezoelectric-assisted photocatalytic systems. As a consequence, piezoelectric and photocatalytic materials are synergistically integrated into direct Z-scheme heterojunction, which both broadens the light absorption range and prolongs carrier lifetimes, and simultaneously expedites the separation and transfer of photogenerated charges [41–45]. This synergy renders piezoelectric effect-assisted Z-scheme heterojunction an ideal choice for an impressive improvement in the PCR.

Here, direct Z-scheme heterojunction ZnIn₂S₄/BaTiO₃ (ZIS/BTO) composite was successfully prepared through a hydrothermal method, exhibiting remarkable efficiency in the PCR. The experimental findings elucidated the collaborative impact of the piezoelectric effect induced by ultrasonic excitation of BTO and the electron transport pathways inherent to the Z-scheme heterojunction structure, synergistically enhancing charge transport and separation. When subjected to visible light irradiation and ultrasonication, ZIS/BTO composite achieved a significant yield of 105.89 μmol g⁻¹ h⁻¹, making an enhancement of 2.55 and 3.62-fold over the individual performance of ZIS and BTO, respectively. This substantial improvement underscores the superior PCR capabilities of piezoelectric effect-assisted Z-scheme heterojunction structure.

2. Experimental

2.1. Materials

All reagents used in this study were of analytical grade and were not further purified, including zinc chloride (ZnCl₂, 98 %, Aladdin), indium chloride tetrahydrate (InCl₃·4H₂O, 99.9 %, Aladdin), thioacetamide (CH₃CSNH₂, 98 %, Aladdin), ethylene glycol (CH₂OH, 98 %, Aladdin), titanium dioxide (TiO₂, 99.8 %, Aladdin), sodium hydroxide (NaOH, 97 %, Aladdin), barium hydroxide octahydrate (Ba(OH)₂·8H₂O, 98 %, Aladdin), hydrochloric acid (HCl, 36–38 %, XiLong Scientific), triethanolamine (C₆H₁₅NO₃, 78–100 %, Aladdin), acetonitrile (CH₃CN, 99 %, Aladdin), Tris(2,2'-bipyridine)dichlororuthenium(II) hexahydrate (C₃₀H₂₄C₁₂N₆Ru·6H₂O, 98 %, Aladdin).

2.2. Catalyst preparation

As reported in the literature, BaTiO₃ was prepared by hydrothermal synthesis [46]. The synthesis process involved two sequential steps. Firstly, TiO₂ was dispersed in a NaOH solution, and the resultant mixture was transported to a reactor and exposed to thermal treatment at of 200 °C for a period of 24 h. Afterwards, the product was cleaned with water and anhydrous ethanol. After drying, the synthesized Na₂Ti₃O₇ was dispersed in a dilute hydrochloric acid solution with stirring and then washed and drying, ultimately yielding H₂Ti₃O₇. In the second step, an appropriate amount of Ba(OH)₂·8H₂O and H₂Ti₃O₇ was added in DI water, and ultrasonic vibration was used to make it dispersed. Finally, the mixed solution was heated to 200 °C for 8 h. The

powder obtained was washed and dried overnight.

BaTiO₃/ZnIn₂S₄ heterojunction was obtained by improving the method reported in the literature [47]. A percentage of ZnCl₂, InCl₃·4H₂O and CH₃CSNH₂ were dissolved in ethylene glycol with vigorous stirring, and then different molar ratios of BaTiO₃ powder materials were uniformly dispersed in the above solution. The solution was transferred to reactor and heated to 120 °C for 2 h. The products were washed, dried, and then received ZnIn₂S₄/BaTiO₃ materials with different ratios (1:0.3, 1:1, 1:1.5). The samples with other BaTiO₃ contents were noted as ZIS/0.3BTO, ZIS/BTO, ZIS/1.5BTO). Pure ZnIn₂S₄ catalysts were prepared by the same method without incorporating BaTiO₃.

2.3. Characterizations

Sample morphology was obtained on a SU8020 (Hitachi, Japan) scanning electron microscope (SEM). The Tecnai G2 F20 (FEI, USA) was used to perform transmission electron microscopy (TEM) in conjunction with energy-dispersive X-ray spectroscopy (EDX). X-ray powder diffraction (XRD) pattern was used to analyze the crystal structure of samples using X'Pert 3 Powder X-ray Diffractometer (Malvern Panalytical, Holland). The UV-vis diffuse reflectance spectra (DRS) of the samples were tested on a UV3600 UV-Vis-NIR Spectrophotometer. The Brunauer-Emmett-Teller (BET) specific surface area (S_{BET}) and pore size distribution of the powders were obtained by Quantachrome Nova 2000e (USA). The Fourier transform infrared (FTIR) spectra were obtained by VERTEX80v (Bruker, German). X-ray photoelectron spectroscopy (XPS) was performed on Thermo Scientific ESCALAB Xi⁺ (USA). Piezo-response scanning force microscopy (PFM) measurements were carried out with Asylum Research MFP-3D-SA. Measurement of photoluminescence (PL) spectra and time-resolved photoluminescence (TRPL) on a FLS-980, full-featured fluorescence spectrometer (Edinburgh, UK).

2.4. PCR performance testing

Typically, a percentage of photocatalyst and Tris(2,2'-bipyridine)dichlororuthenium(II) hexahydrate were dispersed in triethanolamine and acetonitrile (Tris(2,2'-bipyridine)dichlororuthenium(II) hexahydrate acts as a photosensitizer, triethanolamine acts as a hole-trapping agent, and acetonitrile acts as a proton donor), and CO₂ was used for bubbling to bring the photocatalyst to adsorption equilibrium with CO₂ and the solution, and then the solution was transferred to a reactor, and a Xenon lamp (420 nm cut-off filter) as a light source, which was placed above the reactor. Prior to commencing the reaction, it was necessary to evacuate the reaction system to eliminate any air within the reactor, following which high-purity CO₂ was introduced. The reaction time was 6 h, during which samples of the reaction gas were collected at 1 h intervals. These samples were then analyzed using a gas chromatograph (GC-7820) to identify and evaluate the resulting compounds.

2.5. Photoelectrochemical measurements

All electrochemical and photoelectrochemical (PEC) assays were performed on a CHI-660B electrochemical workstation using a quartz electrolytic cell containing a Na₂SO₄ solution. The light source for PEC assays was a 300 W xenon lamp (CEL-HXF300, China).

3. Results and discussion

3.1. Morphological and structural characterization

The morphology of ZIS/BTO heterojunction materials was characterized by scanning electron microscope (SEM) and transmission electron microscopy (TEM). The results showed that ZIS was a 2D nanoflower stacked with ultrathin nanosheets (Fig. 1a and 1d). BTO

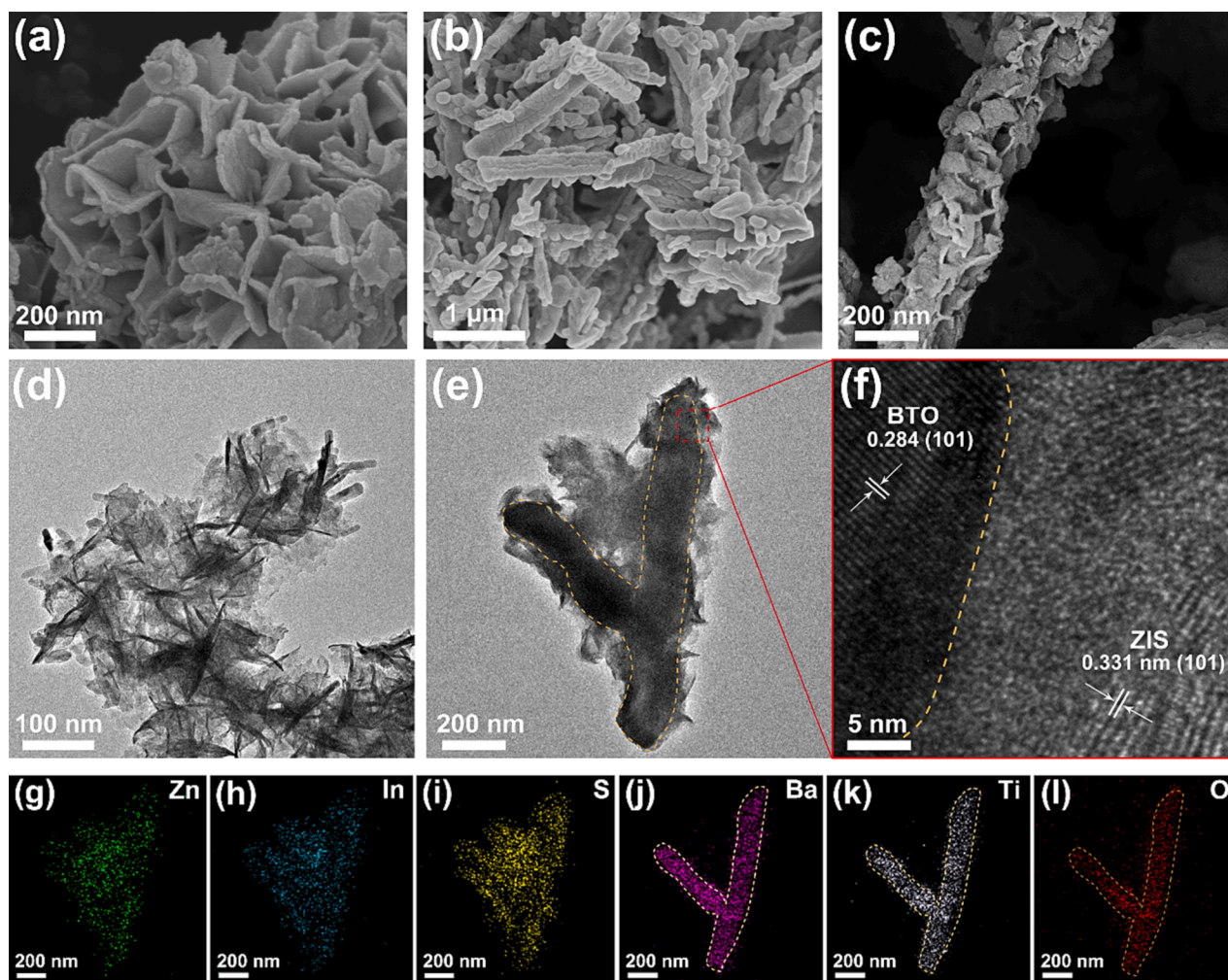


Fig. 1. SEM images of (a) ZIS, (b) BTO and (c) ZIS/BTO. TEM images of (d) ZIS and (e) ZIS/BTO. (f) HRTEM image of the selected area in (e). EDX elemental mapping for (g) Zn, (h) In, (i) S, (j) Ba, (k) Ti and (l) O of ZIS/BTO.

nanowire exhibited an uneven morphology, with a diameter range from 100 to 300 nm and a length spanning 1 to 2 μm (Fig. 1b). ZIS/BTO synthesized by the in-situ growth method was 3D fiber morphology with ZIS nanosheets wrapped around BTO nanowires (Fig. 1c). Furthermore, TEM of the composite showed that ZIS uniformly grew on irregular BTO nanowires (Fig. 1e), verifying the establishment of a proximate interface between ZIS and BTO, which was favorable for shortening the time and distance of electron transfer [48]. High-resolution transmission electron microscopy (HRTEM) images (Fig. 1f) presented clear lattice fringes of ZIS and BTO, with a lattice stripe distance of 0.331 nm corresponding to the (101) face of ZIS with hexagonal phase, and 0.284 nm corresponding to the (101) face of BTO with tetragonal phase. It is noteworthy that there were amorphous regions between the well-crystallized lattice matrices, probably due to the formation of binary homogeneous junctions at the interfaces [34]. Energy Dispersive X-ray spectroscopy (EDX) showed that Zn, In, S, Ba, Ti, and O were uniformly distributed in the ZIS/BTO cross-section, indicating the perfect composite of ZIS and BTO through the heterojunction structure (Fig. 1g-l).

In order to confirm the structure of ZIS/BTO composite, X-ray diffraction (XRD) patterns illustrated in Fig. 2a demonstrated that ZIS showed a hexagonal crystal structure (JCPDS 72-0773) with diffraction peaks at 21.6° , 27° , 28.9° , 47.2° , and 56.3° corresponding to the (006), (101), (008, 103), (110) and (203, 118) crystal planes, respectively, while BTO showed a tetragonal crystal structure (JCPDS 83-1877) with the diffraction peaks at 22.2° , 31.5° , 38.9° , 45.4° , 56.3° , and 65.7° corresponding to the (100), (101), (111), (200), (211), and (202)

crystal planes, respectively. ZIS/BTO heterojunction structure exhibited the presence of both ZIS and BTO phases. In addition, BTO diffraction peaks increased as the BTO concentration grew, and no impurity peaks appeared. These findings validated the successful composite of ZIS and BTO. Furthermore, Fourier transform infrared (FTIR) spectra (Fig. S1) demonstrated that the vibrational signals of the characteristic functional groups belonging to ZIS and BTO at $\sim 600\text{ cm}^{-1}$, $\sim 860\text{ cm}^{-1}$, $\sim 1060\text{ cm}^{-1}$, $\sim 1400\text{ cm}^{-1}$ and $\sim 1615\text{ cm}^{-1}$ simultaneously existed, which further proved the successful composite of ZIS and BTO [49,50].

To deeply investigate the interaction between ZIS and BTO in ZIS/BTO, the optical properties were firstly analyzed by UV-vis diffuse reflectance spectroscopy (UV-vis DRS) in Fig. 2b, showing the absorption boundaries for pure ZIS and BTO at 450 nm and 400 nm, respectively. Besides, ZIS/BTO composite showed a certain degree of red-shift in the absorption edge of ZIS/BTO, and an improved visible light absorption, which was closely related to the decrease of the bandgap of heterogeneous structure between ZIS and BTO and the increase of photo-generated charges. Then, the bandgaps of ZIS, BTO, and ZIS/BTO were calculated from the Kubelka-Munk function to be 2.57 eV, 3.17 eV, and 2.44 eV, respectively (Fig. 2c). Obviously, owing to the narrow-bandgap ZIS and the formation of heterogeneous structure between ZIS and BTO, the bandgaps of ZIS/BTO decrease significantly to 2.44 eV. Subsequently, X-ray photoelectron spectroscopy (XPS) was further used to investigate the chemical state (Fig. S2). XPS high-resolution energy spectra were obtained to investigate the interaction between ZIS and BTO in ZIS/BTO deeply, as shown in Fig. 2d-i. In ZIS, the binding

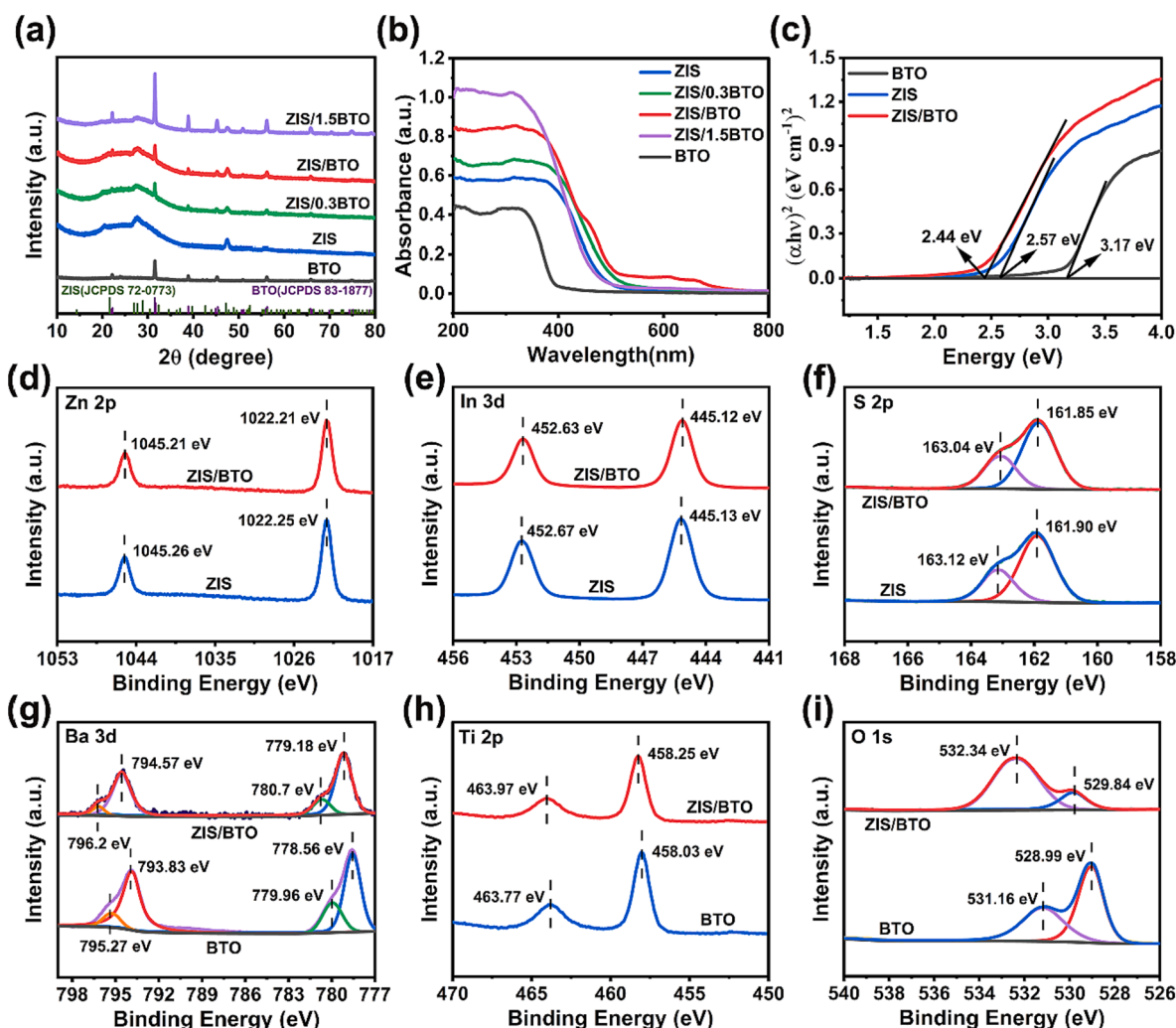


Fig. 2. (a) XRD spectra and (b) UV-vis spectra of samples. (c) Kubelka-Munk function transformed UV-vis spectra of samples. High-resolution XPS spectra of (d) Zn 2p, (e) In 3d, (f) S 2p, (g) Ba 3d, (h) Ti 2p and (i) O 1s.

energies of In $3d_{3/2}$ and $3d_{5/2}$ are 452.67 and 445.13 eV, respectively, which are attributed to the binding state of In^{3+} ; the binding energies of Zn $2p_{1/2}$ and $2p_{3/2}$ are 1045.26 and 1022.25 eV, respectively, and the binding energies of S $2p_{1/2}$ and $2p_{3/2}$ are 161.90 and 163.12 eV, respectively. Upon complexation of ZIS with BTO, Zn 2p, In 3d, and S 2p are all shifted to low binding energies, indicating that ZIS acts as an electron acceptor. The Ba 3d curve of BTO consists of two peaks at 793.83 (Ba $3d_{3/2}$) and 778.56 eV (Ba $3d_{5/2}$) and two satellite peaks, and the Ti 2p curve consists of two peaks at 463.77 (Ti $2p_{1/2}$) and 458.03 eV (Ti $2p_{3/2}$). Notably, the O 1s spectrum of BTO can be divided into two peaks located at 531.16 and 528.89 eV, respectively, which are attributed to the lattice and surface adsorbed oxygen of the Ti-O species, respectively, and the related two peaks in ZIS/BTO are shifted to higher binding energies of 532.34 and 529.84 eV. In contrast to ZIS, the Ba 3d, Ti 2p, and O 1s binding energies of ZIS/BTO are shifted to higher binding energies compared to pure BTO, indicating that BTO acts as an electron donor. As a result, the significant shifts in the XPS spectra showed an intense interaction between ZIS and BTO, thereby demonstrating that surface CO_2 was thermodynamically more favored to bind with surface atoms to increase PCR activity. In addition, the specific surface areas were obtained via N_2 adsorption and desorption (Fig. S3 and Table S1) demonstrated that all three materials had type IV isotherms with H3-type hysteresis loops, implying that the materials were mesoporous (2-50 nm pore diameters) structure. The specific surface areas of ZIS and BTO were 26.039 and 5.71 m^2/g , respectively.

Specially, the growth of ZIS on BTO increased the specific surface area of BTO to 19.685 m^2/g . Hence, the mesoporous structure and high specific surface area of ZIS/BTO composite could supply numerous active sites, thereby enhancing CO_2 adsorption capacity and PCR performance.

3.2. PCR performance

The piezoelectric characteristics of BTO were systematically evaluated by piezo-response force microscopy (PFM). The magnitude-voltage butterfly loop and a phase reversal hysteresis return line of about 180° were revealed in Fig. 3a, indicating that BTO has good piezoelectric properties. Notably, charge migration may be successfully controlled by the piezoelectric potential, which could be a novel auxiliary strategy for improving CO_2 conversion [36]. As can be seen in Fig. S4, the CO_2 reduction performance was optimal and charge separation was maximized when the ultrasonic frequency reached 40 kHz. PCR activity was investigated under light irradiation and light+ultrasonic conditions, respectively. Fig. 3b and Fig. S5a showed that under light condition, the conversion performance of pure ZIS and BTO was poor, and the CO yield was low. Specially, PCR performance of ZIS/BTO composite was significantly improved, which had the best PCR activity. After 6 h of light exposure, the CO yield of ZIS/BTO reached 89.61 $\mu\text{mol g}^{-1} \text{h}^{-1}$, which was 2.16 and 5.69 times higher than that of pure ZIS and BTO, respectively, CH_4 yield too low to be negligible. As illustrated in Fig. 3c and Fig. S5b, after reacting under the combined effect of light and

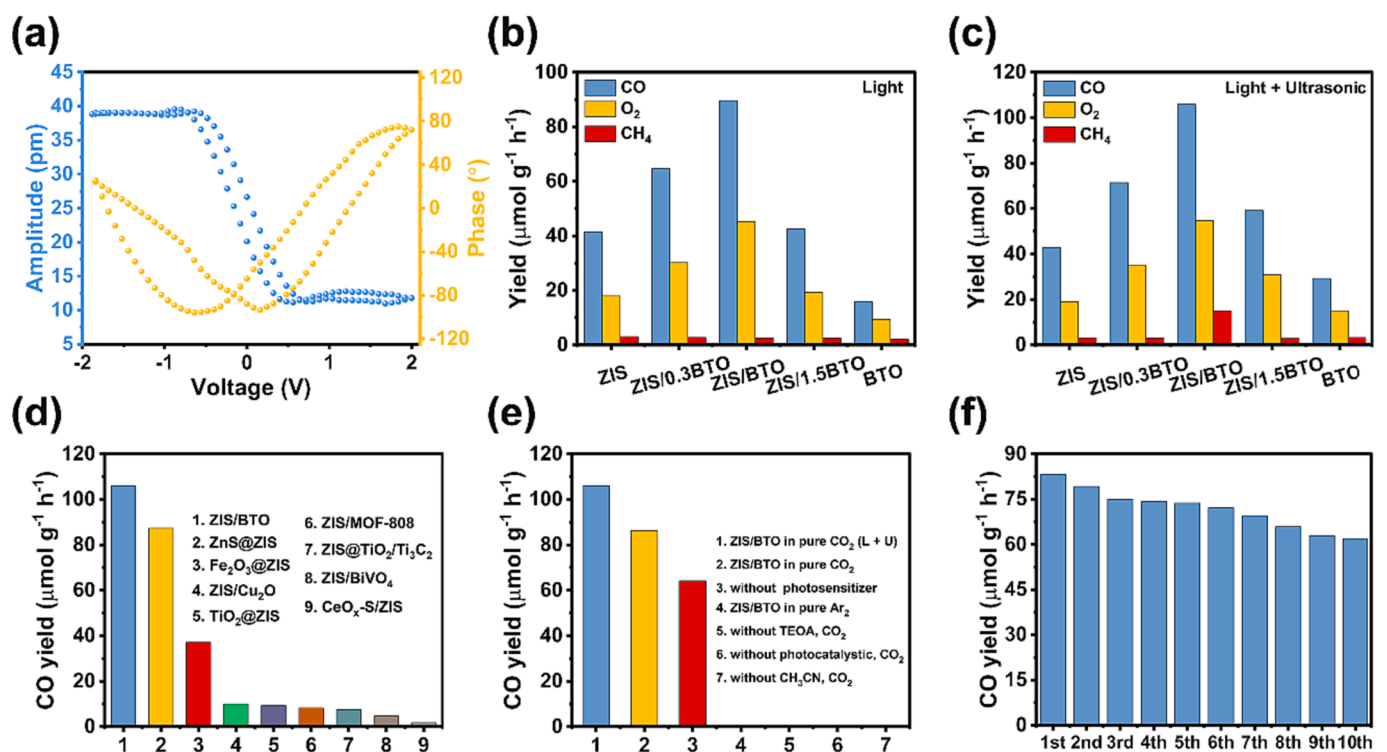


Fig. 3. (a) The displacement-voltage curve and the phase curve of BaTiO₃. Yield of different samples under (b) light and (c) light+ultrasonic, respectively. (d) Comparison of photocatalytic CO₂ reduction performance of ZIS/BTO with other reported ZnIn₂S₄-based heterojunction catalysts. (e) Control experiments and (f) cycling experiments of ZIS/BTO.

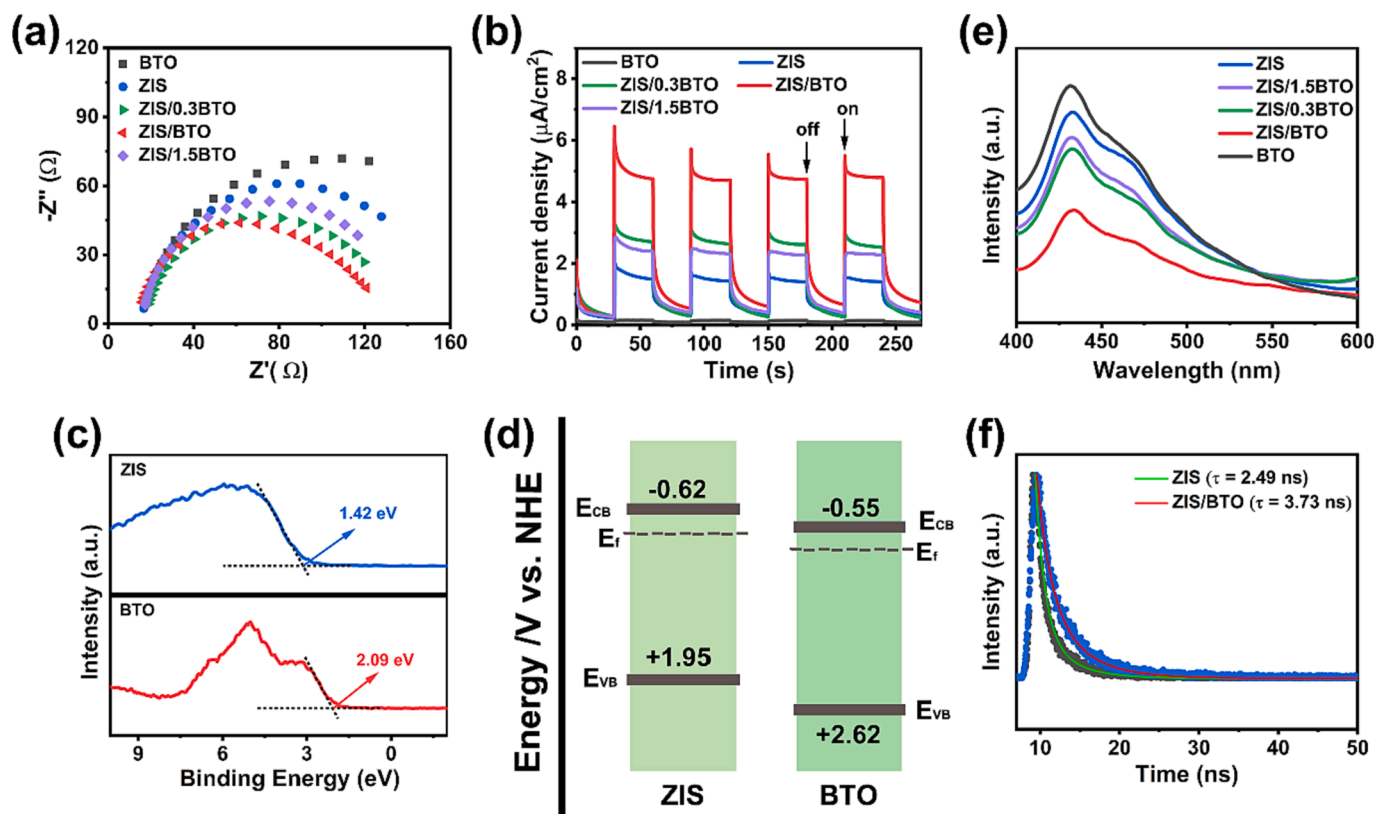


Fig. 4. (a) EIS curves and (b) I-t curves of different samples. (c) VB XPS spectra of ZIS and BTO. (d) Energy band structure diagram of ZIS and BTO. (e) PL spectra of different samples. (f) Time-resolved photoluminescence spectra of ZIS and ZIS/BTO.

ultrasonic for 6 h, the CO yield of ZIS/0.3BTO was enhanced by 10 %, ZIS/BTO by 18 %, ZIS/1.5BTO by 39 %, and BTO by 86 %. At the same time, the CH₄ yield of ZIS/BTO has boosted considerably. Notably, all the samples, except ZIS, showed significant CO yield enhancement and the CO yield gradually increased with more BTO. Furthermore, the O₂ production was also detected with roughly close to stoichiometric molar ratio of CO to O₂ (2:1). These results further demonstrated that ultrasonic can activate the piezoelectric effect of BTO and generate a piezoelectric potential, promoting carrier separation and transfer. In contrast to previous studies of various heterojunction catalysts for PCR performance, ZIS/BTO composite exhibited a remarkably high yield (Fig. 3d and Table S2). Furthermore, the control experiment in Fig. 3e showed that the catalyst, light source, CO₂, and H₂O were essential for the reaction. Cycling experiments in Fig. 3f exhibited that the CO yield did not significantly change under light irradiation after ten cycles of the ZIS/BTO reaction. Moreover, there are no noticeable structural and morphological changes before and after the ZIS/BTO reaction,

indicating the outstanding stability of ZIS/BTO composite (Fig. S6 and S7).

3.3. Photoelectrochemical properties

Electron migration was explored using photoelectrochemical methods. From the electrochemical impedance spectrum (EIS) in Fig. 4a, the arc radius of ZIS/BTO was smaller than that of ZIS and BTO, indicating the improved charge separation of the ZIS/BTO composite. On the contrary, the arc radius of ZIS/BTO was the most minor, indicating that its electrical impedance was the lowest, and the electrons mobility was the highest under light. In addition, the photoelectrochemical I-t curves recorded under light irradiation (Fig. 4b) were carried out to investigate the phototropic electron transport of photocatalysts. In the absence of light, there was practically no current intensity in any of the samples. Under light irradiation, the photocurrent intensity of ZIS/BTO composite was higher than that of pure ZIS and BTO, indicating that the

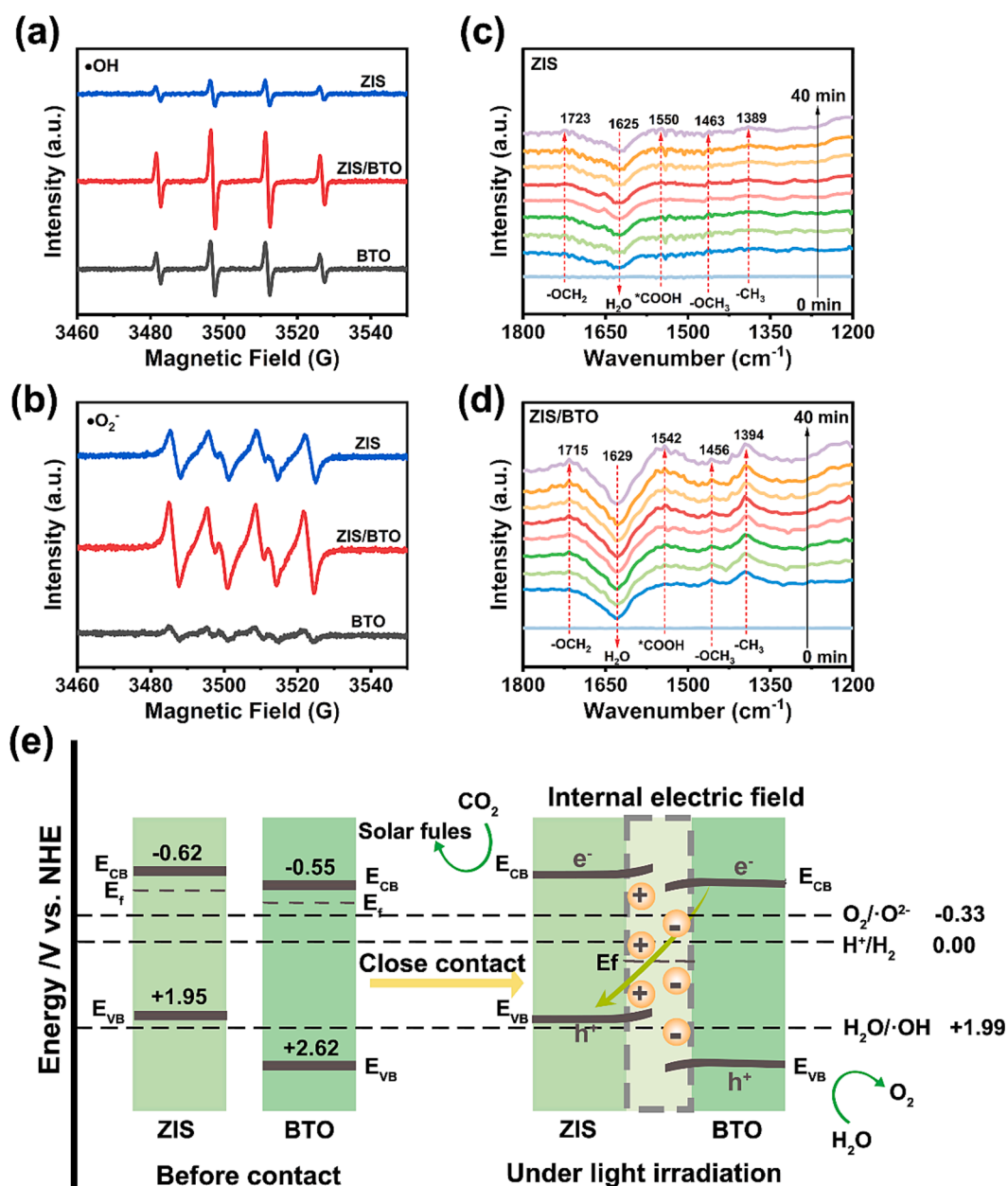


Fig. 5. ESR spectra of (a) •OH and (b) •O₂⁻ adducts over different samples after irradiation. In situ DRIFTS spectra of (c) ZIS and (d) ZIS/BTO. (e) Schematic illustration of photocatalytic CO₂ reduction electron transport mechanism of direct Z-scheme ZIS/BTO heterojunction structure.

composite of ZIS and BTO could promote charge separation and thereby improve CO₂ reduction performance. Among them, ZIS/BTO obtained the highest photocurrent intensity, indicating that the complexation of ZIS and BTO can effectively inhibit electron-hole complexation and promote charge separation. Specially, the excess BTO weakened the photocurrent intensity in ZIS/BTO composite, consistent with the CO₂ conversion results. The energy band structures were obtained by combining the UV-vis DRS spectrum and the valance band X-ray photoelectron spectroscopy (VB XPS). As shown in Fig. 4c-d and Table S3, the valance band maxima (VBM) of ZIS and BTO are 1.95 eV and 2.62 eV, respectively, and the conduction band minima (CBM) of ZIS and BTO could be deduced to be -0.62 eV and -0.55 eV, respectively, which was basically consistent with the conduction band calculated by Mott-Schottky curves (ZIS: -0.63 eV, BTO: -0.54 eV, Fig. S8). Therefore, the electron transfer mechanism of ZIS/BTO heterojunction structure may be type-II or Z-scheme. The fluorescence of ZIS/BTO was greatly suppressed in comparison to ZIS and BTO in the steady-state PL spectra (Fig. 4e), indicating that the ZIS/BTO composite inhibited electron-hole recombination [51]. Furthermore, ZIS and ZIS/BTO were analyzed by time-resolved photoluminescence (TRPL) spectroscopy, it can be seen that the fluorescence lifetime of ZIS is shorter than that of ZIS/BTO, confirming that the introduction of BTO prolongs the lifetime of the photogenerated electronics in ZIS (Fig. 4f and Table S4) [52]. As a result, ZIS/BTO heterojunction structure promotes charge separation and prolongs carrier lifetimes, thereby enhancing CO₂ reduction performance.

3.4. Investigation of photocatalytic mechanism

To deeply validate the electron transfer mechanism of ZIS/BTO composite, electron spin resonance (ESR) experiments were performed for both -OH and -O₂ radicals. According to Fig. 5a-b, both pure ZIS and BTO showed weak -OH and -O₂ signals attributed to the faster compounding of the electron-hole complexes in the single-component samples. Little -OH was produced owing to the insufficient oxidation potential of ZIS to oxidize H₂O to -OH. The presence of a significant quantity of -OH in BTO was observed as a result of its high oxidation potential, in contrast to the large amount of -O₂ found in ZIS due to a high reduction potential. Notably, the stronger -OH and -O₂ signals in ZIS/BTO compared to pure ZIS and BTO suggested that the electron transfer pathway of the ZIS/BTO heterostructure was consistent with a Z-scheme mechanism rather than a type-II mechanism (Fig. 5e). Density-functional theory (DFT) calculations were further conducted to confirm the electron transfer between ZIS and BTO. As shown in Fig. S9, a significant charge transfer occurred at the interface of ZIS/BTO heterostructure. Specially, electrons were more inclined to be transferred from BTO to the ZIS surface, while holes were aggregated in BTO. Thus, ZIS acted as the reduction center and BTO acted as the oxidation center in the ZIS/BTO heterostructure. Combining the theoretical calculations and experimental results, the Z-scheme charge transfer mechanism of the ZIS/BTO heterostructure was verified.

To clarify the reaction pathway and mechanism of CO₂ reduction to CO, in situ diffuse reflectance infrared Fourier transform spectroscopy (DRIFTS) was used to investigate the reaction intermediates of ZIS and ZIS/BTO. Notably, essential intermediates in the CO₂ conversion process (-OCH₂ at 1715 cm⁻¹, *COOH at 1542 cm⁻¹, -OCH₃ at 1456 cm⁻¹, and -CH₃ at 1394 cm⁻¹) could be observed in Fig. 5c-d, demonstrating that CO₂ can be effectively converted at ZIS/BTO heterojunction interface. Under the same conditions, the peaks of intermediaries in ZIS did not change significantly, but the peak intensity was weaker than that of ZIS/BTO, indicating that heterojunction formation can effectively improve the reactivity of PCR. According to the analysis of the intermediates, the CO₂ reduction pathway of ZIS/BTO was the formaldehyde pathway, and the main reaction steps were shown in Table S5.

Based on the above exploration, we put forward a Z-scheme mechanism to elucidate the improved CO₂ reduction efficiency in ZIS/BTO

photocatalysis (Fig. 5e). Specifically, when subjected to visible light excitation, both electrons and holes are generated by ZIS and BTO. These electrons, residing in the CB of ZIS, are efficiently transported across the ZIS/BTO heterojunction interface, where they engage in complexes with holes located in the VB of BTO. By this means, more energetic electrons situated in the CB of ZIS can be applied to CO₂ reduction, whereas the more energetic holes in the VB of BTO are utilized for H₂O oxidation. Consequently, direct Z-scheme heterojunction structure sustains high reduction and oxidation capabilities, thus enhancing the PCR performance.

4. Conclusions

To summarize, direct Z-scheme ZIS/BTO heterojunction structure was successfully prepared by a two-step process, which was driven by simulated sunlight to reduce CO₂. The CO yield of ZIS/BTO was 2.55 and 3.62 times higher than that of pure ZIS and BTO, respectively. This enhancement in performance may be attributed to the Z-scheme heterojunction to generate an intrinsic electric field upon photoexcitation, facilitating Z-scheme carrier transfer between the interfaces of ZIS and BTO. This, mitigates photogenerated electron-hole recombination while preserve superior CO₂ reduction capability of ZIS in the conduction band. In addition, we observed a further boost in the CO yield of ZIS/BTO under reaction conditions that involved both light and ultrasonication. This underlines the pivotal role of the piezoelectric effect, working in synergy with direct Z-scheme electron transfer, in promoting carrier separation and thereby augmenting CO₂ conversion. The combined impact of the piezoelectric effect and the dominant direct Z-scheme heterostructure significantly enhances the performance of PCR, exhibiting a remarkably high yield when compared with previous studies of various heterojunction catalysts. This work offers an innovative approach for harnessing renewable energy sources, such as solar energy and mechanical vibrations, to address the mounting global energy demand and overconsumption of non-renewable fossil fuels.

CRediT authorship contribution statement

Shanyue Lu: Data curation, Formal analysis, Investigation, Methodology, Writing – original draft. **Shengwei Zhang:** Data curation, Formal analysis, Investigation, Methodology, Writing – original draft. **Linlin Li:** Methodology. **Cong Liu:** Project administration, Supervision, Writing – review & editing. **Zhou Li:** Funding acquisition, Project administration, Writing – review & editing. **Dan Luo:** Conceptualization, Funding acquisition, Project administration, Writing – review & editing.

Declaration of competing interest

The authors declare that they have no known competing financial interests or personal relationships that could have appeared to influence the work reported in this paper.

Data availability

No data was used for the research described in the article.

Acknowledgments

This study was supported by the National Key Research and Development Program of China (2021YFB3201200, 2022YFB3205602); National Natural Science Foundation of China (52372174, T2125003, 81971770); Carbon Neutrality Research Institute Fund (CNIF20230204); Natural Science Foundation of Beijing Municipality (L212010); and the Fundamental Research Funds for the Central Universities (E3E46804).

Appendix A. Supplementary data

Supplementary data to this article can be found online at <https://doi.org/10.1016/j.cej.2024.149058>.

References

- [1] J. Ran, M. Jaroniec, S.-Z. Qiao, Cocatalysts in semiconductor-based photocatalytic CO₂ reduction: achievements, challenges, and opportunities, *Adv. Mater.* 30 (7) (2018) 1704649.
- [2] N.-N. Vu, S. Kaliaguine, T.-O. Do, Critical aspects and recent advances in structural engineering of photocatalysts for sunlight-driven photocatalytic reduction of CO₂ into Fuels, *Adv. Funct. Mater.* 29 (31) (2019) 1901825.
- [3] H. Liu, H.-L. Jiang, Solar-Powered Artificial Photosynthesis Coupled with Organic Synthesis, *Chem* 5 (10) (2019) 2508–2510.
- [4] P. Chang, Y. Wang, Y. Wang, Y. Zhu, Current trends on In₂O₃ based heterojunction photocatalytic systems in photocatalytic application, *Chem. Eng. J.* 450 (2022) 137804.
- [5] D. Li, M. Kassymova, X. Cai, S.-Q. Zang, H.-L. Jiang, Photocatalytic CO₂ reduction over metal-organic framework-based materials, *Coord. Chem. Rev.* 412 (2020) 213262.
- [6] H. Huang, H. Song, J. Kou, C. Lu, J. Ye, Atomic-level insights into surface engineering of semiconductors for photocatalytic CO₂ reduction, *J. Energy Chem.* 67 (2022) 309–341.
- [7] X. Chang, T. Wang, J. Gong, CO₂ photo-reduction: insights into CO₂ activation and reaction on surfaces of photocatalysts, *Eng. Environ. Sci.* 9 (7) (2016) 2177–2196.
- [8] P. Li, H. Xu, L. Liu, T. Kako, N. Umezawa, H. Abe, J. Ye, Constructing cubic-orthorhombic surface-phase junctions of NaNbO₃ towards significant enhancement of CO₂ photoreduction, *J. Mater.* 2 (16) (2014) 5606–5609.
- [9] R.-G. Yang, Y.-M. Fu, H.-N. Wang, D.-P. Zhang, Z. Zhou, Y.-Z. Cheng, X. Meng, Y.-O. He, Z.-M. Su, ZIF-8/covalent organic framework for enhanced CO₂ photocatalytic reduction in gas-solid system, *Chem. Eng. J.* 450 (2022) 138040.
- [10] R. de Richter, T. Ming, P. Davies, W. Liu, S. Caillol, Removal of non-CO₂ greenhouse gases by large-scale atmospheric solar photocatalysis, *Prog. Energy Combust. Sci.* 60 (2017) 68–96.
- [11] Y. Ma, S. Wang, X. Duan, Recent advances in direct gas–solid-phase photocatalytic conversion of CO₂ for porous photocatalysts under different CO₂ atmospheres, *Chem. Eng. J.* 455 (2023) 140654.
- [12] H. Yu, C. Sun, Y. Xuan, K. Zhang, K. Chang, Full solar spectrum driven plasmonic-assisted efficient photocatalytic CO₂ reduction to ethanol, *Chem. Eng. J.* 430 (2022) 132940.
- [13] Y. Wang, G. Fan, S. Wang, Y. Li, Y. Guo, D. Luan, X. Gu, X.W. Lou, Implanting CoO_x Clusters on Ordered Macroporous ZnO Nanoreactors for Efficient CO₂ Photoreduction, *Adv. Mater.* 34 (42) (2022) 2204865.
- [14] C.T.K. Nguyen, N. Quang Tran, S. Seo, H. Hwang, S. Oh, J. Yu, J. Lee, T. Anh Le, J. Hwang, M. Kim, H. Lee, Highly efficient nanostructured metal-decorated hybrid semiconductors for solar conversion of CO₂ with almost complete CO selectivity, *Mater. Today* 35 (2020) 25–33.
- [15] C. Bie, B. Zhu, F. Xu, L. Zhang, J. Yu, In Situ Grown Monolayer N-Doped Graphene on CdS Hollow Spheres with Seamless Contact for Photocatalytic CO₂ Reduction, *Adv. Mater.* 31 (42) (2019) 1902868.
- [16] S. Yin, X. Zhao, E. Jiang, Y. Yan, P. Zhou, P. Huo, Boosting water decomposition by sulfur vacancies for efficient CO₂ photoreduction, *Eng. Environ. Sci.* 15 (4) (2022) 1556–1562.
- [17] Z. Zeng, Y. Yan, J. Chen, P. Zan, Q. Tian, P. Chen, Boosting the Photocatalytic Ability of Cu₂O Nanowires for CO₂ Conversion by MXene Quantum Dots, *Adv. Funct. Mater.* 29 (2) (2019) 1806500.
- [18] Y. Xiao, C. Men, B. Chu, Z. Qin, H. Ji, J. Chen, T. Su, Spontaneous reduction of copper on Ti₃C₂T_x as fast electron transport channels and active sites for enhanced photocatalytic CO₂ reduction, *Chem. Eng. J.* 446 (2022) 137028.
- [19] A. Kumar, S. Rana, T. Wang, P. Dhiman, G. Sharma, B. Du, F.J. Stadler, Advances in S-scheme heterojunction semiconductor photocatalysts for CO₂ reduction, nitrogen fixation and NO_x degradation, *Mater. Sci. Semicond. Process.* 168 (2023) 107869.
- [20] E. Karamian, S. Sharifnia, On the general mechanism of photocatalytic reduction of CO₂, *J. CO₂ Util.* 16 (2016) 194–203.
- [21] R. Li, W. Zhang, K. Zhou, Metal-Organic-Framework-Based Catalysts for Photoreduction of CO₂, *Adv. Mater.* 30 (35) (2018) 1705512.
- [22] X. Wang, J. He, X. Chen, B. Ma, M. Zhu, Metal halide perovskites for photocatalytic CO₂ reduction: An overview and prospects, *Coord. Chem. Rev.* 482 (2023) 215076.
- [23] Z.-Y. Chen, N.-Y. Huang, Q. Xu, Metal halide perovskite materials in photocatalysis: Design strategies and applications, *Coord. Chem. Rev.* 481 (2023) 215031.
- [24] Z.-K. Xin, Y.-J. Gao, Y. Gao, H.-W. Song, J. Zhao, F. Fan, A.-D. Xia, X.-B. Li, C.-H. Tung, L.-Z. Wu, Rational Design of Dot-on-Rod Nano-Heterostructure for Photocatalytic CO₂ Reduction: Pivotal Role of Hole Transfer and Utilization, *Adv. Mater.* 34 (3) (2022) 2106662.
- [25] Y. Feng, C. Wang, P. Cui, C. Li, B. Zhang, L. Gan, S. Zhang, X. Zhang, X. Zhou, Z. Sun, K. Wang, Y. Duan, H. Li, K. Zhou, H. Huang, A. Li, C. Zhuang, L. Wang, Z. Zhang, X. Han, Ultrahigh Photocatalytic CO₂ Reduction Efficiency and Selectivity Manipulation by Single-Tungsten-Atom Oxide at the Atomic Step of TiO₂, *Adv. Mater.* 34 (17) (2022) 2109074.
- [26] J. Pi, X. Jia, Z. Long, S. Yang, H. Wu, D. Zhou, Q. Wang, H. Zheng, Y. Yang, J. Zhang, J. Qiu, Surface and Defect Engineering Coupling of Halide Double Perovskite Cs₂NaBiCl₆ for Efficient CO₂ Photoreduction, *Adv. Energy Mater.* 12 (43) (2022) 2202074.
- [27] Y. Zhao, S. Zhang, R. Shi, G.I.N. Waterhouse, J. Tang, T. Zhang, Two-dimensional photocatalyst design: A critical review of recent experimental and computational advances, *Mater. Today* 34 (2020) 78–91.
- [28] P. Sharma, A. Kumar, G. Zheng, T. Mashifana, P. Dhiman, G. Sharma, F.J. Stadler, Current scenario in ternary metal indium sulfides-based heterojunctions for photocatalytic energy and environmental applications: A review, *Mater. Today Commun.* 36 (2023) 106741.
- [29] X. Zheng, Y. Song, Y. Liu, Y. Yang, D. Wu, Y. Yang, S. Feng, J. Li, W. Liu, Y. Shen, X. Tian, ZnIn₂S₄-based photocatalysts for photocatalytic hydrogen evolution via water splitting, *Coord. Chem. Rev.* 475 (2023) 214898.
- [30] J. Low, J. Yu, M. Jaroniec, S. Wageh, A.A. Al-Ghamdi, Heterojunction Photocatalysts, *Adv. Mater.* 29 (20) (2017) 1601694.
- [31] P. Zhou, J. Yu, M. Jaroniec, All-Solid-State Z-Scheme Photocatalytic Systems, *Adv. Mater.* 26 (29) (2014) 4920–4935.
- [32] Y. Yuan, R.-T. Guo, L.-F. Hong, X.-Y. Ji, Z.-D. Lin, Z.-S. Li, W.-G. Pan, A review of metal oxide-based Z-scheme heterojunction photocatalysts: actualities and developments, *Mater. Today Energy* 21 (2021) 100829.
- [33] D. Huang, S. Chen, G. Zeng, X. Gong, C. Zhou, M. Cheng, W. Xue, X. Yan, J. Li, Artificial Z-scheme photocatalytic system: What have been done and where to go? *Coord. Chem. Rev.* 385 (2019) 44–80.
- [34] J. Li, F. Wei, Z. Xiu, X. Han, Direct Z-scheme charge transfer of Bi₂WO₆/InVO₄ interface for efficient photocatalytic CO₂ reduction, *Chem. Eng. J.* 446 (2022) 137129.
- [35] Z.L. Wang, Nanopiezotronics, *Adv. Mater.* 19 (6) (2007) 889–892.
- [36] L. Pan, S. Sun, Y. Chen, P. Wang, J. Wang, X. Zhang, J.-J. Zou, Z.L. Wang, Advances in Piezo-Photonic Effect Enhanced Photocatalysis and Photoelectrocatalysis, *Adv. Energy Mater.* 10 (15) (2020) 2000214.
- [37] S. Wang, Z. Li, G. Yang, Y. Xu, Y. Zheng, S. Zhong, Y. Zhao, S. Bai, Embedding Nano-Piezoelectrics into Heterointerfaces of S-Scheme Heterojunctions for Boosting Photocatalysis and Piezophotocatalysis, Small n/a(n/a) (2023) 2302717.
- [38] C. Hu, H. Huang, F. Chen, Y. Zhang, H. Yu, T. Ma, Coupling Piezocatalysis and Photocatalysis in Bi₄NbO₈X (X = Cl, Br) Polar Single Crystals, *Adv. Funct. Mater.* 30 (7) (2020) 1908168.
- [39] C. Wang, C. Hu, F. Chen, T. Ma, Y. Zhang, H. Huang, Design strategies and effect comparisons toward efficient piezocatalytic system, *Nano Energy* 107 (2023) 108093.
- [40] Q. Zhang, Y. Jia, W. Wu, C. Pei, G. Zhu, Z. Wu, L. Zhang, W. Fan, Z. Wu, Review on strategies toward efficient piezocatalysis of BaTiO₃ nanomaterials for wastewater treatment through harvesting vibration energy, *Nano Energy* 113 (2023) 108507.
- [41] C. Zhang, N. Li, D. Chen, Q. Xu, H. Li, J. He, J. Lu, The ultrasonic-induced-piezoelectric enhanced photocatalytic performance of ZnO/CdS nanofibers for degradation of bisphenol A, *J. Alloy. Compd.* 885 (2021) 160987.
- [42] Q. Han, S. Du, Y. Wang, Z. Han, H. Li, H. Xu, P. Fang, Direct Z-scheme MoSe₂/TiO₂ heterostructure with improved piezoelectric and piezo-photocatalytic performance, *J. Colloid Interface Sci.* 622 (2022) 637–651.
- [43] W. Shen, N. Li, S. Zuo, M. Wu, G. Sun, Q. Li, M. Shi, J. Ma, Remarkably enhanced piezo-photocatalytic performance of Z-scheme Bi₂WO₆/Black TiO₂ heterojunction via piezoelectric effect, *Ceram. Int.* 48 (11) (2022) 15899–15907.
- [44] X. Zhang, C. Hu, Z. Zhu, Y. Zhang, S. Tu, Y. Zhang, T. Ma, F. Chen, H. Huang, Efficient piezo-photocatalysis of OD/2D α-Fe₂O₃/Bi₂WO₆: Synergy of weak force-driven piezoelectric polarization and Z-scheme junction, *J. Colloid Interface Sci.* 650 (2023) 1536–1549.
- [45] Y. Fu, Z. Ren, J. Wu, Y. Li, W. Liu, P. Li, L. Xing, J. Ma, H. Wang, X. Xue, Direct Z-scheme heterojunction of ZnO/MoS₂ nanoarrays realized by flowing-induced piezoelectric field for enhanced sunlight photocatalytic performances, *Appl. Catal.* 285 (2021) 119785.
- [46] Q. Liu, D. Zhai, Z. Xiao, C. Tang, Q. Sun, C.R. Bowen, H. Luo, D. Zhang, Piezo-photoelectronic coupling effect of BaTiO₃@TiO₂ nanowires for highly concentrated dye degradation, *Nano Energy* 92 (2022) 106702.
- [47] G. Yang, D. Chen, H. Ding, J. Feng, J.Z. Zhang, Y. Zhu, S. Hamid, D.W. Bahnemann, Well-designed 3D ZnIn₂S₄ nanosheets/TiO₂ nanobelts as direct Z-scheme photocatalysts for CO₂ photoreduction into renewable hydrocarbon fuel with high efficiency, *Appl. Catal.* 219 (2017) 611–618.
- [48] J. Tian, Z. Zhao, A. Kumar, R.I. Boughton, H. Liu, Recent progress in design, synthesis, and applications of one-dimensional TiO₂ nanostructured surface heterostructures: a review, *Chem. Soc. Rev.* 43 (20) (2014) 6920–6937.
- [49] S. Wang, Q. Li, S. Sun, K. Ge, Y. Zhao, K. Yang, Z. Zhang, J. Cao, J. Lu, Y. Yang, Y. Zhang, M. Pan, Z. Lin, L. Zhu, Heterostructured ferroelectric BaTiO₃@MOF-Fe/Co electrocatalysts for efficient oxygen evolution reaction, *J. Mater.* 10 (10) (2022) 5350–5360.
- [50] M. Tan, Y. Ma, C. Yu, Q. Luan, J. Li, C. Liu, W. Dong, Y. Su, L. Qiao, L. Gao, Q. Lu, Y. Bai, Boosting Photocatalytic Hydrogen Production via Interfacial Engineering on 2D Ultrathin Z-Scheme ZnIn₂S₄/g-C₃N₄ Heterojunction, *Adv. Funct. Mater.* 32 (14) (2022) 2111740.
- [51] Y.-X. Pan, Y. You, S. Xin, Y. Li, G. Fu, Z. Cui, Y.-L. Men, F.-F. Cao, S.-H. Yu, J. B. Goodenough, Photocatalytic CO₂ Reduction by Carbon-Coated Indium-Oxide Nanobelts, *J. Am. Chem. Soc.* 139 (11) (2017) 4123–4129.
- [52] J. Wu, L. Xiong, Y. Hu, Y. Yang, X. Zhang, T. Wang, Z. Tang, A. Sun, Y. Zhou, J. Shen, Z. Zou, Organic half-metal derived erythroid-like BiVO₄/hm-C₆N₃ Z-Scheme photocatalyst: Reduction sites upgrading and rate-determining step modulation for overall CO₂ and H₂O conversion, *Appl. Catal.* 295 (2021) 120277.